IEEE Access
Multidisciplinary ⋮ Rapid Review ⋮ Open Access Journal

Received 29 January 2023, accepted 7 February 2023, date of publication 10 February 2023, date of current version 27 February 2023.

Digital Object Identifier 10.1109/ACCESS.2023.3243957

METHODS

A Priori Information and Off-Axis Measurements in Terahertz Tomography

KARL H. MAY[1,2], ANDREAS KEIL[1,3], (Member, IEEE), GEORG VON FREYMANN[1,2], AND FABIAN FRIEDERICH[1,2]

[1]Fraunhofer Institute for Industrial Mathematics ITWM, 67663 Kaiserslautern, Germany
[2]Research Center OPTIMAS, Department of Physics, Technische Universität Kaiserslautern, 67663 Kaiserslautern, Germany
[3]Becker Photonik GmbH, 32457 Porta Westfalica, Germany

Corresponding author: Karl H. May (karl.henrik.may@itwm.fraunhofer.de)

ABSTRACT Terahertz tomography is a non-contact inspection technique to image objects from multiple angles and reconstruct their 3D volume from intensity and time-of-flight transmission data, without the need for radiation protection measures. Unlike X-rays, terahertz radiation is subject to strong diffraction and refraction when propagating through dielectric materials, which often deteriorate the image reconstruction quality. Our solution to this problem applies ray tracing, considering the beam shape and an *a priori* model of the sample under investigation to predict the beam paths of the terahertz radiation. We present two reconstruction methods based on the resulting beam path predictions yielding higher image quality. Method 1 filters out beams deviating strongly, thus removing induced artifacts and errors from the reconstruction image. Method 2 employs off-axis measurements that acquire data along the full detection plane and in this way detect even strongly deflected beams. Considering these beams and the information they carry in the reconstruction enhances the image quality. Applying these methods to terahertz tomography, even complicated structures can be imaged. We display the significant enhancements achieved with the two methods by comparing the reconstruction results of different polymeric samples.

INDEX TERMS Terahertz radiation, computed tomography, non-destructive testing, a priori information, off-axis measurement, reconstruction algorithms, imaging, time-of-flight, conjugate gradient least square (CGLS).

I. INTRODUCTION

Terahertz radiation (0.1THz − 10THz) enables a wide range of applications in the field of non-invasive testing and imaging [1], [2], [3], [4]. Contactless measurements and, in contrast to X-Ray inspection, the absence of radiation protection requirements make terahertz scanning techniques an important addition to current inspection practices [5]. Typical applications in an industrial context are non-destructive layer thickness determination and defect detection using volumetric imaging [6], [7], [8], [9], [10]. Materials of interest range from ceramics, glass-fiber reinforced composites [2] and plastics [6] over paints and coatings [9] to paper [11] and wood [12].

The associate editor coordinating the review of this manuscript and approving it for publication was Yi Zhang.

Many imaging geometries create a volumetric scan of the sample under test by measuring in a reflection setup with access to only one side of the sample. These approaches sometimes suffer from image distortion and artifacts due to optical effects occurring often at complicated sample structures. Moreover, potentially concealed areas behind other sample features, or generally a lack of radiation power in certain geometric configurations can lead to errors and artifacts when imaging with one-sided approaches. Especially for additively manufactured [13] or extruded objects [14], such as window profiles, performing a full terahertz transmission tomography on the sample from many different angles can be beneficial. For an overview of tomographic techniques applying terahertz radiation, refer to [15] and [16].

In classical X-Ray transmission tomography, projections of an object under test are acquired from different angles and a volume reconstruction is performed which is

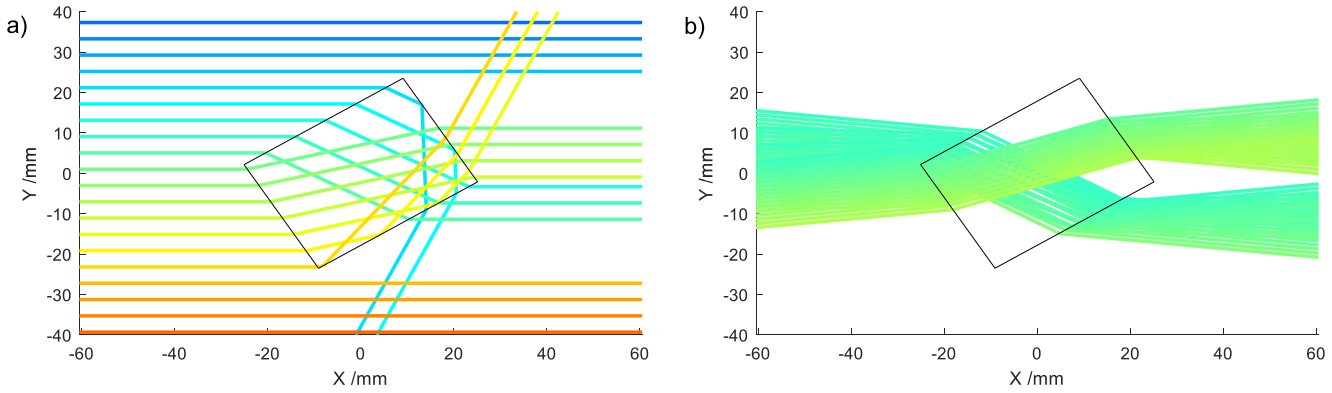

FIGURE 1. Ray tracing simulation of terahertz beam paths (a) assuming infinitely small ray diameters and (b) considering the Gaussian beam shape (one ray iconsists of many thin rays). The density of the plotted beams is reduced in comparison to the simulations to improve visibility.

predicated on the Fourier-slice theorem [17]. A practical and fast algorithm for this reconstruction is the filtered back-projection (FBP), assuming that the radiation travels through the sample in straight lines. For tomography using X-rays applied in a medical or NDT context, this is usually a good assumption. In contrast to X-ray radiation, terahertz radiation is subject to significant diffraction and refraction, due to its larger wavelength. Additionally, the wavelength of terahertz radiation (in the mm to sub-mm range) is of the same order of magnitude as the typical features of the samples, often leading to a deflection from its straight path (see Fig. 1). In this work we introduce a measurement setup, which detects radiation passing through the imaging scene on a straight line and also acquires data *off-axis* to take beams into account that are deflected by the sample. The information carried by these beams would otherwise be lost.

To utilize the full data set, we resort to a versatile, flexible problem formulation, and an iterative reconstruction algorithm to solve it. We apply the conjugate gradient least square (CGLS) algorithm, a robust and efficient method to solve tomography problems iteratively. It has been applied to terahertz tomography for the first time in [18]. It solves large linear systems quickly and offers the possibility to apply constraints to the reconstruction space to improve the reconstruction. The CGLS algorithm solves the inverse problem of the simple matrix multiplication

$$\bar{A}\vec{x} = \vec{b} \tag{1}$$

where the vector $\vec{b}$ contains the measurement data and $\vec{x}$ represents the unknown reconstruction. The matrix $\bar{A}$ contains information about how the radiation travels through the imaging scene. Since $\bar{A}$ is derived from a physical model, this formulation allows incorporating *a priori* information about the measurement system and the sample into the reconstruction process and thus, improves reconstruction quality and resolution. Modeling the sample *a priori* is a common tool in the field of NDT, to assure the quality of objects made out of a well-known material by either extraction or additive manufacturing based on a geometric model. Prior works

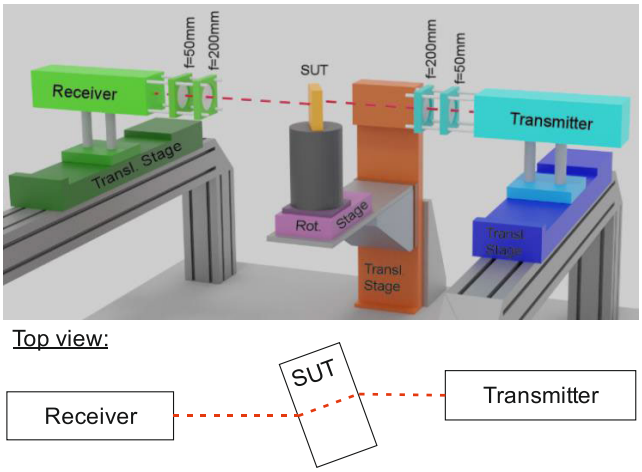

FIGURE 2. Measurement setup with rotational stage (purple) and a linear stage (orange) to turn and move the sample (yellow) in z-direction. Two independent translational stages for receiver (blue) and transmitter (green) allow the acquisition of deflected and non-deflected radiation. The radiation is collimated and focused by the lens pairs in front of the transmitter/receiver units. The dashed red line indicates a possible beam path.

on enhancing the imaging capabilities of different tomographic reconstruction techniques based on *a priori* information can be found for microwave tomography in [19], [20], [21], [22], and [23], for X-Ray tomography in [24], and in the context of terahertz tomography in [25], [26], and [27]. Ding et al. [19] distinguish between two categories of *a priori* information: The first category represents information about the target or sample, such as internal or external boundaries or regions and the respective refractive indices [20], [21], [22], [24]. The second category considers the measurement system, i.e. the number and position of antennas or information about the background [23]. In this work, we suggest a method for the integration of *a priori* information from both categories into the reconstruction formulation. In section IV-C. the data stemming from the off-axis

measurements are used to improve the reconstruction images even further.

II. MEASUREMENT SETUP

The measurement system is a single-pixel setup with one transmitter and one receiver as shown in Fig. 2. The transmitter, consisting of a voltage-controlled oscillator and several active frequency multipliers, continuously emits a frequency-modulated continuous-wave (FMCW) signal in the range from 230 GHz to 320GHz from a Pickett-Potter horn antenna. The beam is collimated by a $f = 50$ mm lens and focused to the center of the setup by a $f = 200$ mm lens. The receiver has the same lens configuration as the transmitter, focusing the radiation into the detector antenna. The lenses have an aperture of $2''$, which was found to be a good trade-off between resolution and illumination for the samples we used. To image larger samples, it is possible to use lenses with a larger aperture, broadening the beam. The receiver consists of a subharmonic mixer, mixing the local oscillator signal with the transmitted radiation, acquiring the signal amplitude and phase coherently. This way, the signal attenuation and the time delay caused by traversing the sample are measured. The mathematical model of the signal after passage through the sample is shown in the next section. The transmitter and receiver are each positioned on separate translation stages allowing an independent movement on the Y-axis perpendicular to the signal propagation direction. This way, not only radiation traveling straight through the imaging scene but also deflected beams can be detected performing off-axis measurements. Furthermore, the setup features a rotational stage to turn the sample under test and another translation stage to lift or lower the sample. By combining cross-sectional images (B-scans) acquired at different heights, a full 3D reconstruction of a sample can be created.

III. A PRIORI INFORMATION

A. MATHEMATICAL MODEL OF TRANSMISSION TOMOGRAPHY

Tomographic imaging of dielectric objects reconstructs the complex refractive index

$$n(x_i) = n'(x_i) + in''(x_i) \tag{2}$$

at each pixel $x_i \in I$ in the discretized image area I. The time-of-flight (ToF) delay T_R of a terahertz signal R traversing through an imaging scene is proportional to $(n_i'(x_i) - n_{\text{air}})$:

$$T_R = \frac{1}{c_0} \sum\nolimits_{i \in I_R} \left(n_i' - n_{\text{air}}\right) |\vec{x}_i| \tag{3}$$

where c_0 is the vacuum speed of light, and $\vec{x}_i$ represents the path through the pixels x_i in the subset $I_R \subset I$ the Ray R traverses. In the following, the refractive index of air is approximated with $n_{\text{air}} \approx 1$. For a given beam the relative intensity loss τ_R due to absorption is according to Lambert-Beer's law:

$$\tau_R = \left|\frac{I}{I_0}\right|_R = \exp\left(-\sum_{i \in I_R} \alpha_i |\vec{x}_i|\right) \tag{4}$$

where $\alpha_i = 4n_i'' \pi f / c_0$ represents the absorption coefficient and f is the frequency of the radiation. In a logarithmic representation of the intensity, measured at a given rotation angle ϑ at a distance d from the center of rotation, (4) can be simplified to

$$\tau_{ln}(\vartheta, d) = \ln(\tau_R) = -\sum_{i \in I_R} \alpha_i |\vec{x}_i| = \sum_{i \in I} \vec{A}_i \cdot I_i^{\tau} \tag{5}$$

The last expression represents a product of the image vector $\vec{I^{\tau}}$ consisting of the entries α_i for every pixel of the imaging scene with the Matrix $\bar{A}$ comprised of the column vectors $\vec{A}_i(\vartheta, d)$, defining which pixels contribute to which ray to which extent. The α_i represent the material absorption coefficient α_{mat} at the pixel position. This model does not take losses due to reflection at surfaces into consideration.

Similarly to (5), (3) can be expressed as:

$$T_R(\vartheta, d) = \sum_{i \in I} \vec{A}_i \cdot I_i^T \tag{6}$$

Here, the same matrix $\bar{A}$ is utilized to calculate the distribution of $n'(x)$ in the imaging area by solving $\bar{A} \cdot \vec{I^T} = \vec{T}(\vartheta, d)$ for $\vec{I^T}$ and $\bar{A} \cdot \vec{I^{\tau}} = \vec{\tau}(\vartheta, d)$ for $\vec{I^{\tau}}$.

This model assumes the medium to be non-dispersive, i.e. $n'(x)$ is independent of frequency. $\vec{T}(\vartheta, d)$ and $\vec{\tau}(\vartheta, d)$ represent the vectors containing the measurement data, namely the ToF and intensity sinograms, respectively. These formulas were derived and discussed in detail in [18], [28], [29], and [30].

The forward problem of terahertz tomography can thus be described by a simple matrix multiplication

$$\bar{A}\vec{x} = \vec{b} \tag{7}$$

with the vector $\vec{b}$ denoting the sinogram of the measurement data, the unknown vector $\vec{x}$ representing the image to be reconstructed and the matrix $\bar{A}$ mapping the image pixels to the corresponding sinogram entries. The latter contains the trajectories of the rays describing how the terahertz rays travel through the measurement area. To calculate these trajectories and thereby model the tomographic process as accurately as possible, *a priori* information about the measurement system and sample under test can be incorporated into the design of $\bar{A}$.

B. OPTICAL EFFECTS OF THE SAMPLE BOUNDARIES

The first category of *a priori* information we consider takes the geometry of the sample under test and its real refractive index n' into consideration. The information about the surface boundaries of the sample under test is used for ray tracing simulations including optical effects like refraction and

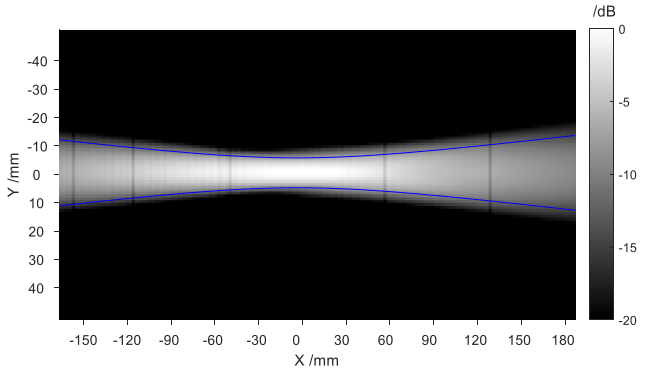

FIGURE 3. Intensity distribution of the beam due to the lens system. The X-axis represents the axial direction, the Y-axis is the radial direction. (Compare Fig. 1 (b)). The blue lines indicate the theoretical boundaries of a Gaussian beam (defined by an intensity decay to $1/e^2$ of the value on the beam axis) for a wavelength of $\lambda = 1$ mm and a focus beam width of $w_0 = 5.2$ mm.

reflection (depicted in Fig. 1). If a simulated ray path intersects with the sample, the diversion of the beam trajectory at the sample boundary is calculated according to Snell's law:

$$n_1' \sin(\varepsilon_1) = n_2' \sin(\varepsilon_2) \tag{8}$$

where ε_1 and ε_2 are the incident angle and the angle of the refracted beam, respectively, both measured towards the surface normal. n_1' and n_2' are the real refractive indices of the two materials, that form the boundary. For an incident angle of

$$\varepsilon \geq \varepsilon_c = \arcsin\left(\frac{n_2'}{n_1'}\right) \tag{9}$$

the critical angle, total internal reflection causes the beam to be reflected at the surface. Whether it is refracted or reflected, the new propagation direction of the beam is calculated. After simulating the necessary beam paths for all transmitter positions, the resulting trajectories are incorporated into the design of the matrix $\bar{A}$ (see section IV-A).

C. BEAM SHAPE

The shape of the beam influences the measurement data and can be considered when reconstructing an image [25]. The lens system of the measurement setup (see Fig. 2) focuses the terahertz radiation into the center of the setup. To measure the beam shape, the receiver is placed onto an X/Y-translation stage, allowing it to move in the axial direction and perpendicular to it. The beam pattern is shown in Fig. 3. The beam profile can be modeled as a Gaussian beam, whose intensity distribution depends on the distance from the beam axis r and the distance from the focus point z as follows:

$$I(r,z) = I_0 \left(\frac{w_0}{w(z)}\right)^2 \exp\left(-\frac{2r^2}{w^2(z)}\right) \tag{10}$$

where I_0 is the maximum intensity at the focal point, and

$$w(z) = w_0 \sqrt{1 + \left(\frac{z}{z_R}\right)^2} \tag{11}$$

Algorithm 1 Ray Tracing Algorithm Returning the Beam Paths $\vec{x}_{\mathbf{l}}^{\mathbf{i},\boldsymbol{\theta}}$

```
for θ = 1 ... N_θ
  for i = 1 ... N
    determine d⃗_l^{i,θ}
    for l = 0 ... l_max
      t = 0
      determine t_hit > 0 values for B_scene and B_SUT
      if x⃗_l^{i,θ} (min(t_hit)) = B_SUT
        determine x⃗_{l+1,0}^{i,θ} = x⃗_l^{i,θ} (t_hit)
        determine d⃗_{l+1}^{i,θ} from equation (8)
      else if x⃗_l^{i,θ} (min(t_hit)) = B_scene(−x_bound)
        discard x⃗_{0...l}^{i,θ}; break
      else if x⃗_l^{i,θ} (min(t_hit)) = B_scene(±y_bound) and d⃗_l^i · e⃗_x < 0
        discard x⃗_{0...l}^{i,θ}; break
      else
        break
    end
  end
end
return all x⃗_l^{i,θ}
```

determines the radius of the beam at any distance z from the focus. w_0 is the center beam waist and $z_R = \frac{\pi w_0^2}{\lambda}$ is the Rayleigh length.

The two blue lines in Fig. 3 indicate the $1/e^2$ intensity expected from the Gaussian beam model with a center wavelength of $\lambda = 1$ mm. The focus beam width of 5.2 mm was found by fitting the theoretical curve to the data. This corresponds to a Rayleigh range of 85mm.

The measured intensity agrees well with the theoretical distribution, indicating that the Gaussian beam shape is a good approximation for the given beam intensity distribution. The beam shape enters the construction of the matrix $\bar{A}$ by including multiple infinitely small elementary beams that lie within the propagation of the full beam as indicated in Fig. 1 (b).

IV. RECONSTRUCTION TECHNIQUES

A. RAY TRACING AND CONSTRUCTION OF $\bar{A}$

By utilizing *a priori* information, we improve the matrix $\bar{A}$ in comparison to the standard design, which only assumes straight and infinitely thin rays. To do so, just as for conventional algorithms the matrix entry a_{ij} represents the length of the path the i-th ray travels in the j-th pixel P_j of the imaging area. Since the beam paths are influenced by the material parameters, the rays do not propagate straight through the sample and thus, the full matrix cannot be calculated in one step. Due to the finite diameter of the Gaussian beam, we build up one wide beam out of several infinitely thin elementary beams. The ray tracing algorithm to determine the trajectories of these elementary beams is described in the follwing.

The pseudo-code for the ray tracing can be found in Algorithm 1. Every part l of an elementary ray i is defined

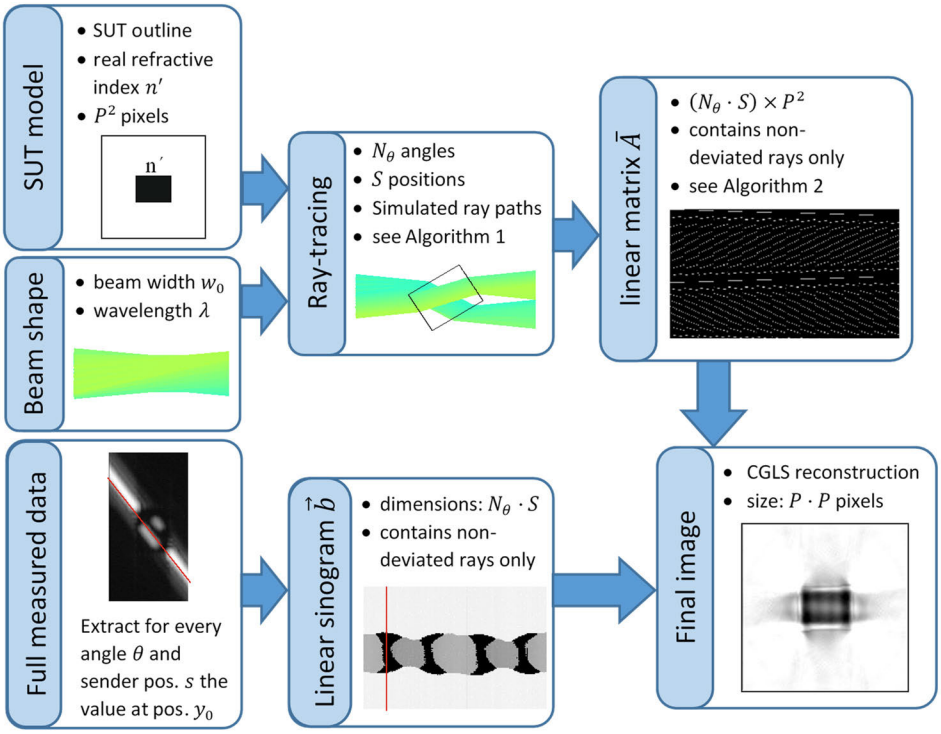

FIGURE 4. Method 1 (a priori): Image reconstruction considering a priori information, filtering out deflected beam paths.

by its start position $\vec{x}^i_{l,0}$ and its direction $\vec{d}^i_l$:

$$\vec{x}^i_l(t) = \vec{x}^i_{l,0} + t \cdot \vec{d}^i_l \tag{12}$$

The propagation of the ray is represented by an increase of the parameter t. By finding the intersections of (12) with the given boundaries of the sample under test (SUT) B_{SUT} and the imaging scene B_{scene} and calculating the respective t values, one can find the first boundary the ray intersects with – represented by the lowest positive t_{hit}. If this boundary corresponds to the imaging scene bounding box, the ray propagation is completed and we continue with the next ray. Otherwise, if a sample surface boundary is reached, we calculate the new start position $\vec{x}^i_{l+1,0} = \vec{x}^i_l(t_{\mathrm{hit}})$ and the new $\vec{d}^i_{l+1}$ according to (8). This procedure is repeated until l reaches $l_{\max}$. To avoid infinite loops, we limit the maximum amount of reflection/refraction incidents to $l_{\max} = 5$, after that the ray is discarded. This was found as a suitable choice considering the strong absorption such a ray would experience due to the long distance of travel. A ray is also discarded if it coincides with the back boundary of the imaging window ($x_{\mathrm{bound}} = -60$ mm in Fig. 1), or if it is heading towards it when leaving the imaging scene bounding box. In Fig. 1(a) we see two strongly diverted blue beams which will be discarded and three yellow beams which will be kept since their trajectories can be extrapolated to finally reach the detector plane. This procedure is repeated for all rays $i = 1 \ldots N$ and for all angles $\theta = 1 \ldots N_\theta$.

In order to account for the Gaussian beam shape of the rays and finally build the matrix $\bar{A}$, we follow Algorithm 2. For every sender and receiver position $s = 1 \ldots S$, we consider the elementary rays, that lie within the Gaussian beam (see Fig. 1). The definitions of the maximum beam width w_{max} and the angle extrema θ_{min} and θ_{max} can be found in the appendix.

Defining the Gaussian beam as a sum of multiple elementary beams does not describe the beam perfectly, but it is an approximation that serves our purposes. In particular, the linear relations between the sinogram value $\vec{\tau}/\vec{T}$ and the distance $\vec{x}$ traveled in the imaging scene in (5) and (6) are preserved by this approach.

B. METHOD 1:A PRIORI

The inclusion of the *a priori* information presented above leads to an improved model of the forward problem of tomography represented by (7). This approach, here called method 1, shares some similarities with [27]: When constructing the matrix $\bar{A}$ from the trajectories simulated by our Ray tracing algorithm (Algorithm 2), we include the deflected beam paths by connecting the measurement value in the sinogram with the pixels the deflected beam passes. Hereby, in this first method, we include only rays, whose trajectories end at a position, that is covered by the aperture of the receiver placed at the same position on the Y-axis as the transmitter. Therefore, only rays with a maximum deflection of 25mm from the receiver and sender position y_0 are considered, while all other rays are ignored. In contrast to [27] we only take the

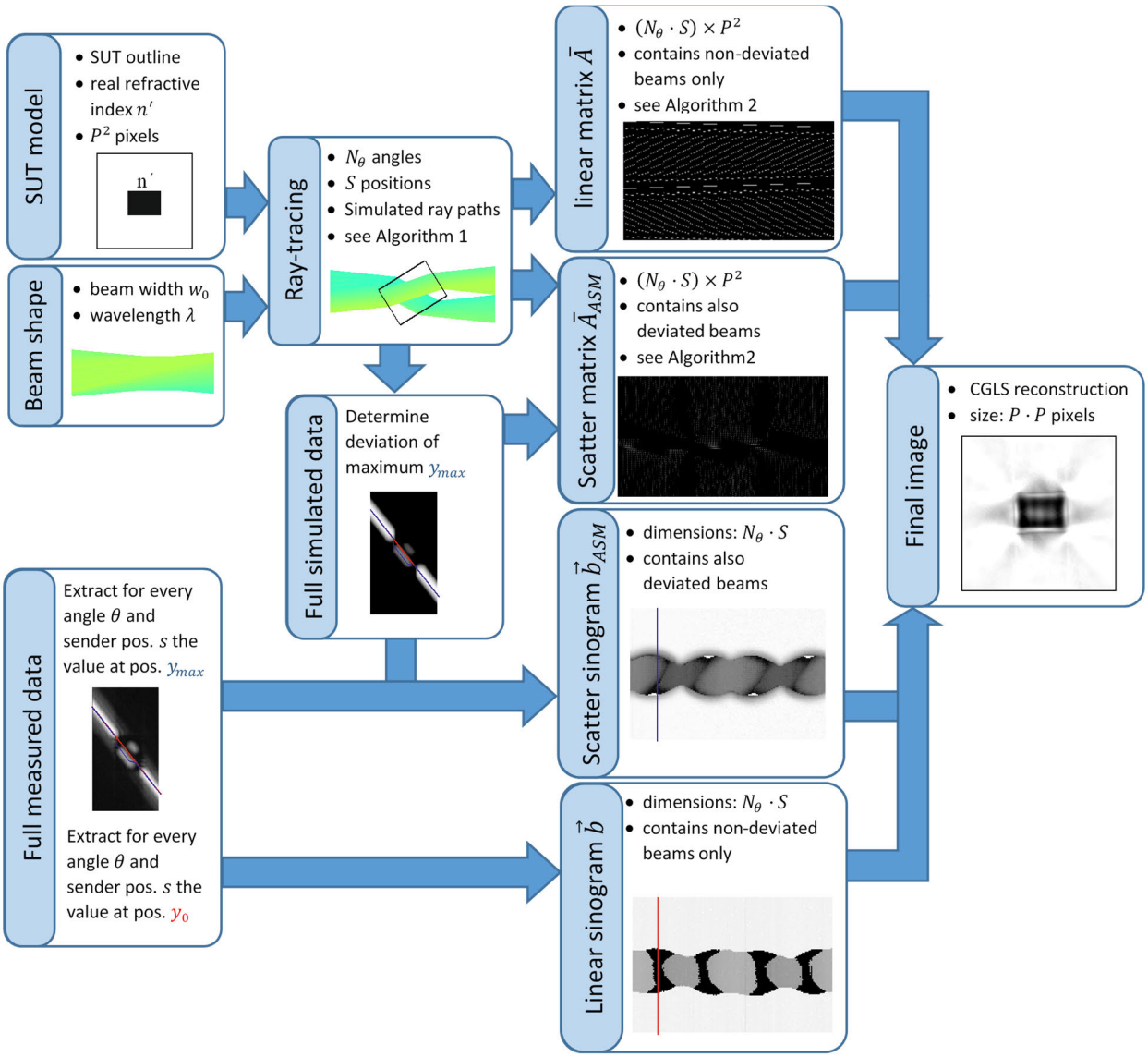

FIGURE 5. Method 2 (a priori + off-axis): Image reconstruction considering a priori information using deflected beams.

outer surface boundaries of the samples into account, when performing the ray tracing simulations. This way we can also reconstruct defects and features of the sample, whose existence was *a priori* not known. This reconstruction procedure, schematically depicted in Fig. 4, allows the reconstruction of samples from measurement data resulting from a parallel movement of sender and receiver, placing them in front of each other at any time. Alternatively, the sinogram $\vec{b}$ can be extracted from a full off-axis measurement by creating projections along the diagonal $y_{\text{trans}} = y_{\text{reic}}$, where the position of the transmitter equals the position of the receiver on the opposite side of the beam axis. The diagonal is indicated in Fig. 4 by the red line in the lower left full data block. Following this procedure for every angle θ yields the sinogram $\vec{b}$. Since strongly deflected beams do not pass the receiver aperture, the information they carry is lost. This can induce errors in the reconstruction, especially when reducing the density of the measured angles to increase the measurement speed. Therefore, we introduce the second reconstruction method, also considering these strongly deflected beams.

C. METHOD 2:A PRIORI + OFF-AXIS

The second method is schematically depicted in Fig. 5. As indicated in section II, we designed the measurement setup allowing an independent movement of the transceiver and receiver unit, rendering the detection of strongly deflected radiation possible. For every transmitter position, we move the receiver off-axis along its full range of motion spanning 400 mm. For a measurement resolution of 0.5 mm for the receiver unit and 1 mm for the transmitter range of 120 mm, this leads to a full data block of 800 × 120 values for every angle for a single cross-sectional image. It is schematically

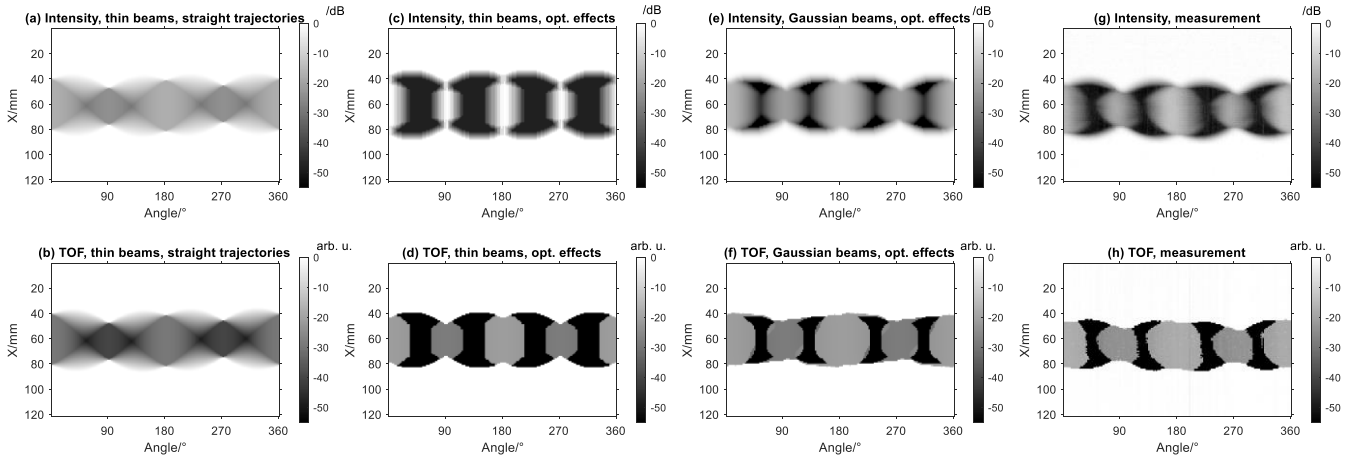

FIGURE 6. Comparison of sinograms; (a), (b) simulated without a priori information; (c), (d) including optical effects on the sample boundaries; (e), (f) full a priori information (Gaussian beam shape and opt. effects); (g), (h) measured data of Sample 1(a); intensity and time-of-flight (ToF).

Algorithm 2 Calculating the Reconstruction Matrices $\bar{A}$ and $\bar{A}_{ASM}$ (Additional Scatter Matrix Including a *Priori* Information). See Also Appendix.

```
for s = 1 ... S:
  for i = 1 ... N:
    get trajectory x⃗^{i,θ} from Algorithm 1
    calculate distance d = |x⃗^{i,θ}_{0,0} − y_0(s)|
    if d ≤ w(−x_bound)
      calculate θ_min(d) and θ_max(d) from A.(15)
      for θ = θ_min ... θ_max
        if |end(x⃗^{i,θ}) − y_0(s)| ≤ w(x_bound)
          a_ij = lenght(x⃗^{i,θ} ∩ P_j)
        end
        if |end(x⃗^{i,θ}) − y_max(s)| ≤ w(x_bound)
          a^ASM_ij = lenght(x⃗^{i,θ} ∩ P_j)
        end
      end
    end
  end
end
return Ā, Ā_ASM
```

depicted in the lower-left corner of Fig. 5 and contains the attenuation and time-of-flight (ToF) information of all, including strongly deflected, beams, provided their incident angle is not too steep to pass the detector optics. Based on the ray tracing simulations including the *a priori* information about the sample under test and the beam shape, we simulate these data blocks for every measurement angle. From the simulated data, we determine the receiver position $y_{\max}(s)$ in the detector plane, where we expect most radiation to be detected. The value intensity and ToF value of $y_{\max}$ are denoted in the scatter sinogram $\vec{b}_{\mathrm{ASM}}$, where ASM stands for *additional scatter matrix*. The beam pixels associated with all the beams reaching the aperture of the receiver at the position $y_{\max}$, are denoted in the scatter matrix $\bar{A}_{\mathrm{ASM}}$, following Algorithm 2. Finally, we combine both matrices and both sinograms and analogously to method 1 apply the CGLS algorithm to solve the inverse problem and reconstruct the image $\vec{I}$:

$$\begin{pmatrix} \bar{A} \\ \bar{A}_{\mathrm{ASM}} \end{pmatrix} \cdot \vec{I} = \begin{pmatrix} \vec{b} \\ \vec{b}_{\mathrm{ASM}} \end{pmatrix} \tag{13}$$

y_{max} and b_{ASM} contain the information of the strongly deflected beams about the object's internal structure. However, they might be prone to errors due to possible deviations of the model from the real measurement process. We found that combining $(\bar{A}, \bar{A}_{\mathrm{ASM}})$ and (b, b_{ASM}) yields better results than reconstructing from either of the pairs solely.

Even though (13) is twice the size of the original problem (e.g. (7)), its inversion can still be solved within seconds, thanks to the excellent performance of the CGLS algorithm, which is explained in the next section.

D. CONJUGATE GRADIENT LEAST SQUARE (CGLS) ALGORITHM

In literature, there exists a large variety of methods to tackle inverse problems, such as (7) and (13). For an overview, refer to [28] and [33]. While some are based on statistical approaches like the Bayesian methods, others, the so-called "row-action" methods like algebraic reconstruction technique (ART) or Split-Bregman method [31], consider the matrix one row at a time. The latter option performs typically slow on large matrices. In this work we utilize the conjugate gradient least square algorithm (CGLS), which iterates towards an optimal solution following conjugate gradients. It performs fast and efficiently, even on the typically large and non-square system matrices of the tomography problem.

The CGLS algorithm has been covered extensively in [32], [33], and [34] and in the context of terahertz tomography in [18]. Here, we will give a brief outline of the main idea.

The CGLS algorithm is an iterative algorithm for approximating the solution x_i of an inverse problem such as (7), for a known positive-definite (not necessarily square) matrix $\bar{A}$ and an also known measurement vector $\vec{b}$. It does so by

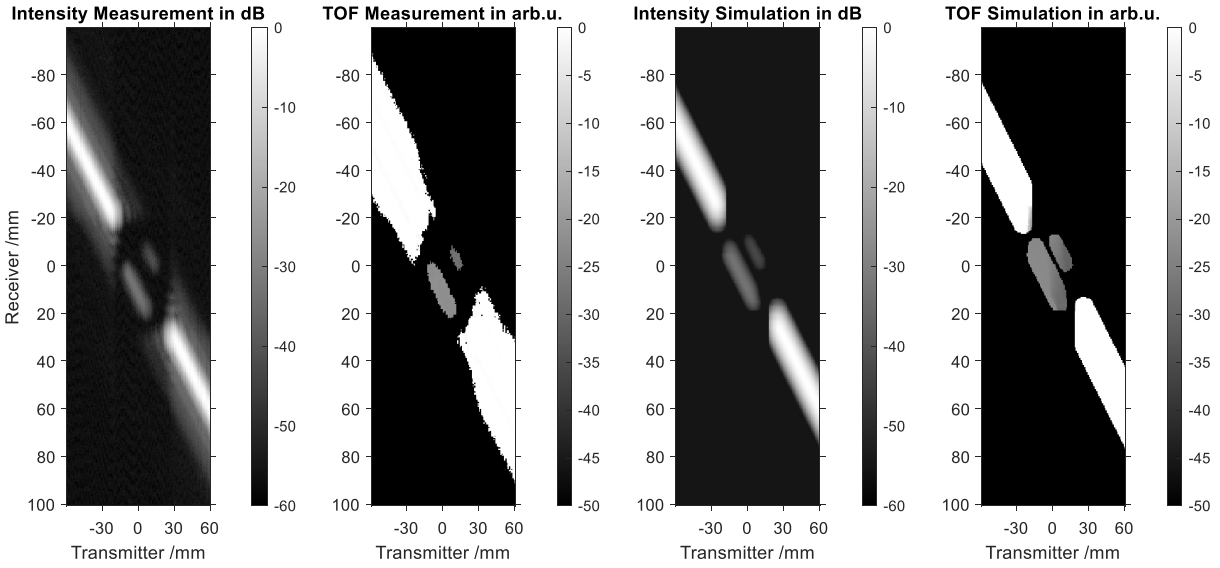

FIGURE 7. Off-axis measurement and corresponding simulation of Sample 1(a) for $\theta = 50°$.

updating an initially given solution x_0 going in steps, which are all $\bar{A}^T\bar{A}$-conjugate to each other. This way, CGLS iterates towards the optimal solution of the problem, provided that the measurement vector is noiseless. When noise is present, the CGLS algorithm becomes semi-convergent, i.e. after finding the optimal solution, it continuous iterating often deteriorating the result. Therefore, one has to apply regularization measures. This can be done by limiting the solution space (for example restriction to R^+) or stopping the iteration process before deterioration starts. The right number of iterations to stop at can be found by applying the L-curve criterion [18], [35]. The reconstructions obtained by applying the CGLS algorithm in combination with the above-mentioned reconstruction methods are displayed in the following section.

V. RESULTS AND DISCUSSION

A. EXPERIMENT DESCRIPTION

To test the capabilities of the different reconstruction methods, we designed three different samples displayed in Fig. 8, Fig. 11, and Fig. 13. Samples 1 and 2 are cuboids of $30 \times 40 \times 60$ mm^3 made from Polyvinyl chloride (PVC) and Polymethylmethacrylate (PMMA), respectively. Sample 3 consists of a $25 \times 75 \times 75$ mm^3 block made from Polyethylene (PE). The optical parameters of the three materials at 300 GHz are indicated in Table 1.

TABLE 1. Optical properties of the used materials [36].

Material	PVC	PMMA	PE
α_{mat} (@300GHz)	0.25 mm^{-1}	1.0 mm^{-1}	< 0.005 mm^{-1}
n_{mat} (@300GHz)	1.69	1.59	1.52

Each sample was constructed twice. Holes were drilled into one specimen serving as artificial defects so that every sample exists in a version (a) without defects and a version (b) with defects. In the case of Sample 1(b) (Fig. 8) and 2(b) (Fig. 11), the defects consist of three concentric holes with diameters of 3, 4, and 5 mm placed with center distances of 8.5 mm and 7.5 mm, respectively. The defect of Sample 3(b) (Fig. 13) has the shape of a pill with a width of 10 mm and a length of 50 mm.

Projections of the samples were acquired in the angle range [0°, 358°] in steps of 2°. When taking optical effects into account, it is important to cover the whole circumference and not only the half-space of 180°, since the resulting sinograms do not necessarily have rotational symmetry. For every angle position, the transmitter unit is moved along the sample in steps of 1 mm (for example over a width of 120 mm, depending on the size of the sample). The receiver unit continuously acquires data moving along its full range of 40cm with a step size of 0.5 mm. This procedure results in a data set of 800×120 data points for every angle, the relevant subset of which is shown exemplarily for Sample 1(a) in Fig. 7.

B. SIMULATION VALIDATION

Before discussing the reconstruction results, we compare the simulated data with the measurements, in order to verify that the inclusion of the *a priori* information improved the model of the measurement process. Fig. 6(a)-(f) show the sinograms resulting from ray tracing of Sample 1(a) (see section IV-A above). Fig. 6(g),(h) show the corresponding measured sinograms. The upper row of Fig. 6 displays the intensity sinograms while the data in the lower one represents the ToF. The simulated sinograms 6(a) and 6(b) assume straight ray trajectories and infinitely thin beams – the standard configuration for (X-ray) tomography. Apart from a factor, the two sinograms are identical, since all rays travel on straight trajectories interacting proportionally to the path length they travel through the sample. This is not the case for Fig. 6(c) and (d) displaying the simulated sinograms when

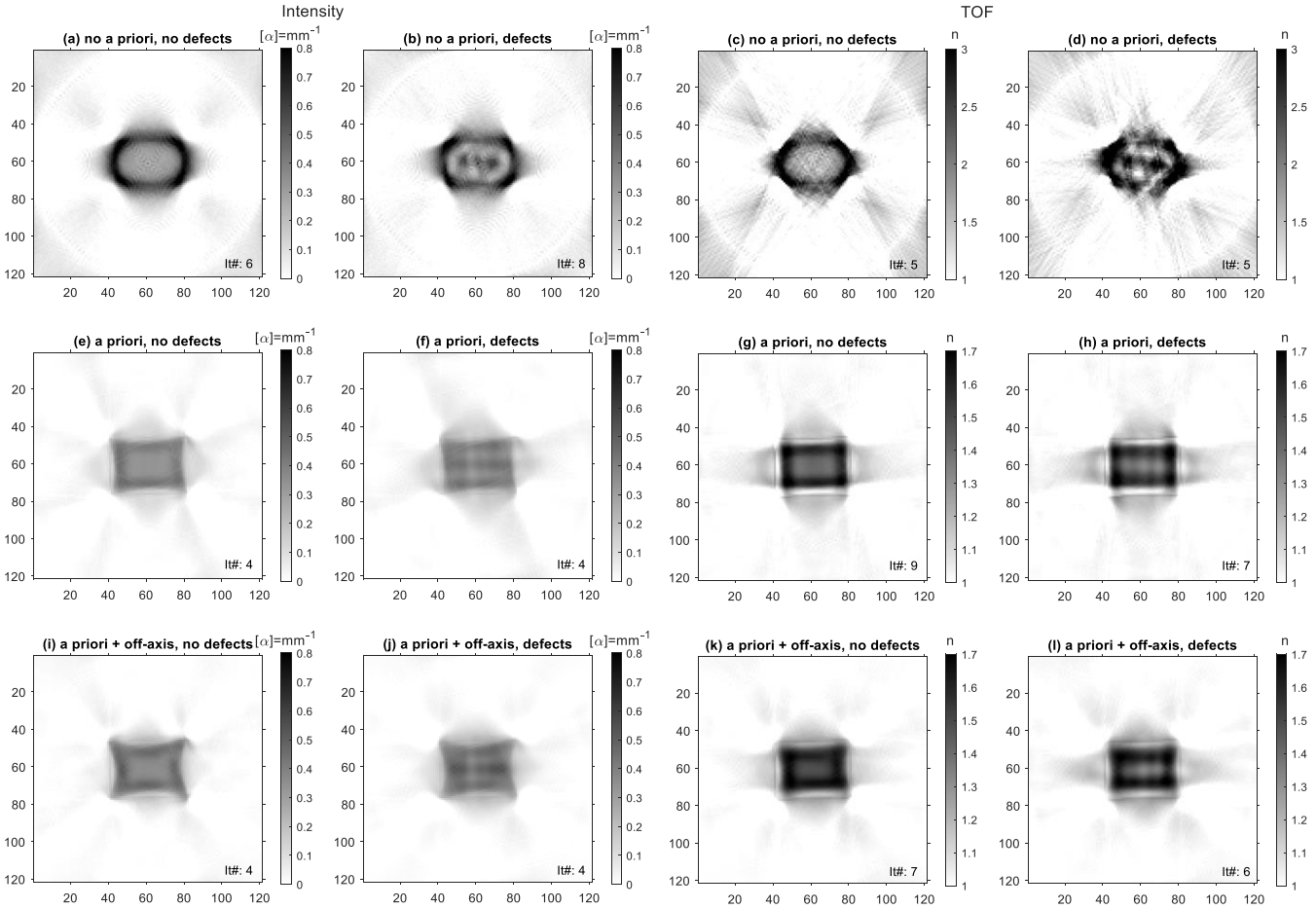

FIGURE 8. Reconstructions of the absorption coefficient α (a,b,e,f,I,j) and the real refractive index n (c,d,g,h,k,l) of Sample 1(a) and 1(b) made out of PVC. X- and Y-axis in mm. The reconstructions where performed without a priori information (a)-(d), with method 1 considering beam shape and optical effects (e)-(h), with method 2 additionally considering scattered radiation from off-axis measurements (i)-(l). Iteration numbers of the CGLS reconstruction algorithm are given in the lower right corner.

refraction and reflection are considered. The simulations take the surface boundaries and the refractive index of the sample as *a priori* information, assuming thin rays. Following the simulation shown in Fig. 1(a), for specific angles 'blind areas' appear, where no radiation reaches the detector aperture. They are visible in all following sinograms as dark areas around the angles $\theta_{i\in N} = 45° + i \cdot 90°$, where the radiation is mainly deflected by the sample. In Fig. 6(c) and (d) said areas are too large and too sharp in comparison with Fig. 6(g) and (h) since in the experiment the beam has a Gaussian shape and therefore a finite radius (see section III-C). This fact is considered in Fig. 6(e) and (f), where both the optical effects as well as the beam shape are regarded as *a priori* information. As a result, the 'blind areas' become smaller and less sharp, since due to the larger beam radius some radiation can still circumvent sharp corners of the sample and reach the detector aperture. Overall, by considering both sets of a priori information the sinograms Fig. 6(e) and (f) are in very good agreement with the measured data as seen in Fig. 6(g) and (h). This promises good reconstruction results because it shows that the most prominent effects influencing the measurement process have been identified and considered.

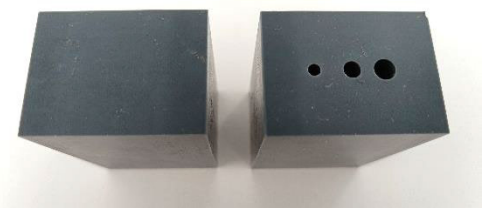

FIGURE 9. Photography of Sample 1(a) and 1(b) made from Polyvinylchlorid (PVC): 30 mm × 40 mm × 60 mm (b) hole diameters: 3, 4, and5 mm.

Similarly, we compare the results from the off-axis measurements and the corresponding simulations. Fig. 7. shows the data resulting from an off-axis measurement of Sample 1(a) at an angle of 50°. The transmitter was moved from −60 mm to 60 mm and the receiver along its full range of motion from −200 mm to 200 mm. To increase visibility, the y-axis was adjusted here to display only the relevant data range. The two graphs on the right side display the corresponding simulated data from the ray tracing procedure.

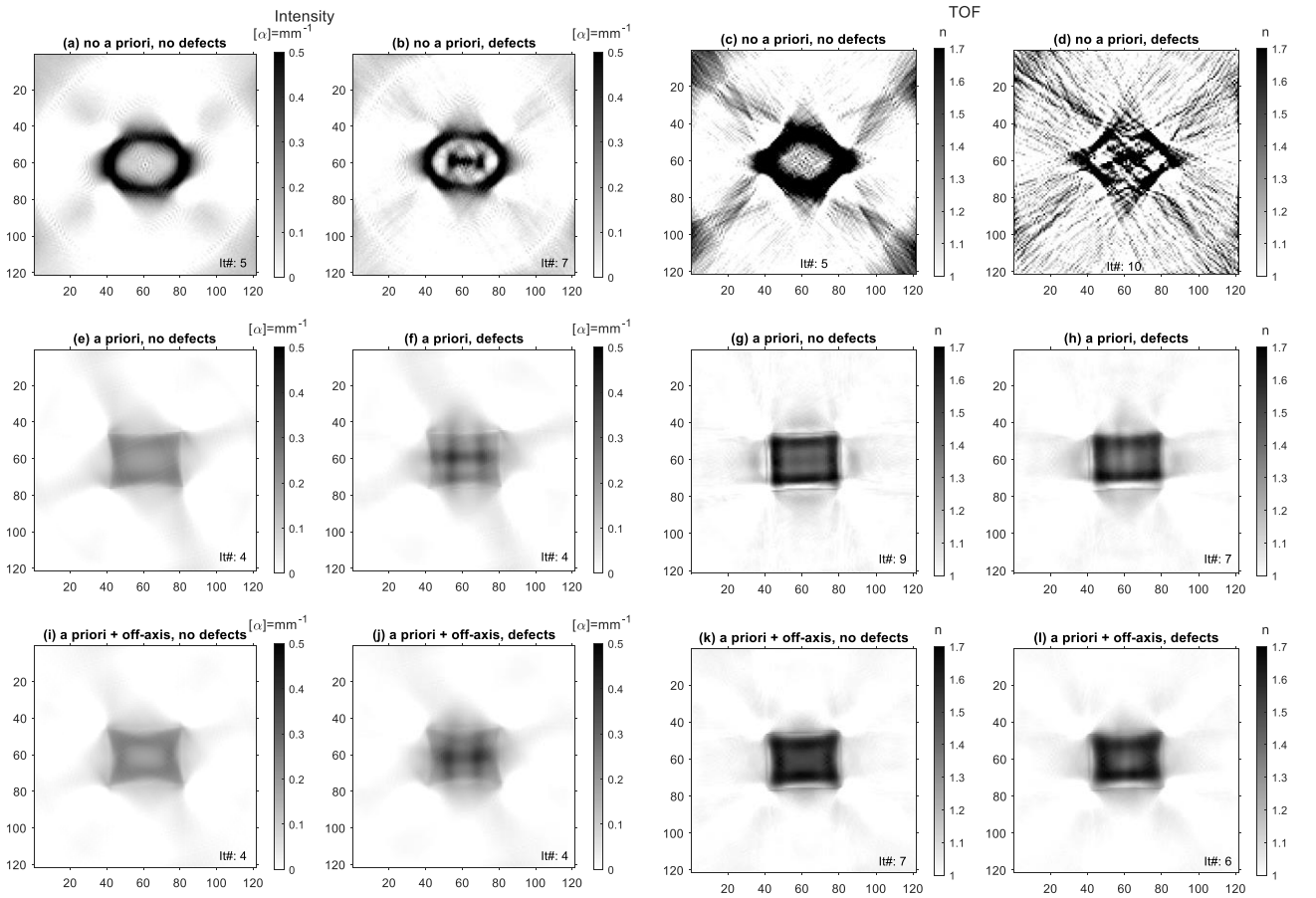

FIGURE 10. Reconstructions of the absorption coefficient α (a,b,e,f,I,j) and the real refractive index n (c,d,g,h,k,l) of Sample 2(a) and 2(b) made out of PMMA. X- and Y-axis in mm. The reconstructions where performed without a priori information (a)-(d), with method 1 considering beam shape and optical effects (e)-(h), with method 2 additionally considering scattered radiation from off-axis measurements (i)-(l). Iteration numbers CGLS reconstruction algorithm are given in the lower right corner.

The bright areas in the $x = y$ diagonal correspond to the radiation traveling from the transmitter directly into the receiver unit. The ToF, or more specifically the time delay induced by the target, is 0 since the beams do not interfere with the sample under test. The intensity reaches values around 0 dB here, indicating maximum transmittance. In the central part, however, where the sample is placed, the radiation is split into two parts, very much in accordance with Fig. 1(b). Here the actual interaction between the radiation and the sample becomes evident – in the form of a reduction of intensity and an increase of the ToF, respectively. Around the edges of the sample there are dark areas indicating that, due to scattering effects, less radiation enters the receiver unit. Fig. 7 shows a good agreement between measurement and simulation as well, justifying the model for the forward problem and the assumptions and simplifications we make. This is crucial for the success of reconstruction method 2 since it uses the off-axis simulations to find the position of maximum radiation intensity $y_{\max}$.

C. IMAGE RECONSTRUCTIONS

The reconstructions of the six samples with the two reconstruction methods described in sections IV-B. and IV-C. are displayed in Fig. 9, Fig. 10, and Fig. 12. The respective number of iterations of the CGLS algorithm is given in the lower right corner of every reconstruction.

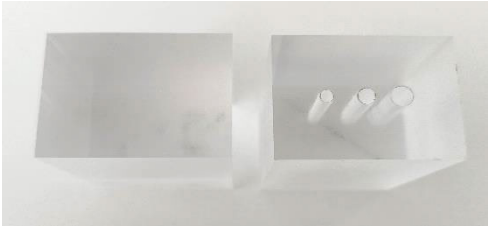

FIGURE 11. Photography of Sample 2(a) and 2(b) made from Polymethylmethacrylat (PMMA): 30 mm × 40 mm × 60 mm (b) hole diameters: 3, 4, and5 mm.

1) SAMPLE 1

Fig. 9 depicts the reconstructions of Samples 1(a) and (b) made from PVC. The first row Fig. 9(a)-(d) shows the reconstructions with the CGLS algorithm utilizing the standard matrix without regarding any *a priori* information. The reconstructions from the intensity data as well as from the ToF data indicate how the refraction and scattering effects are

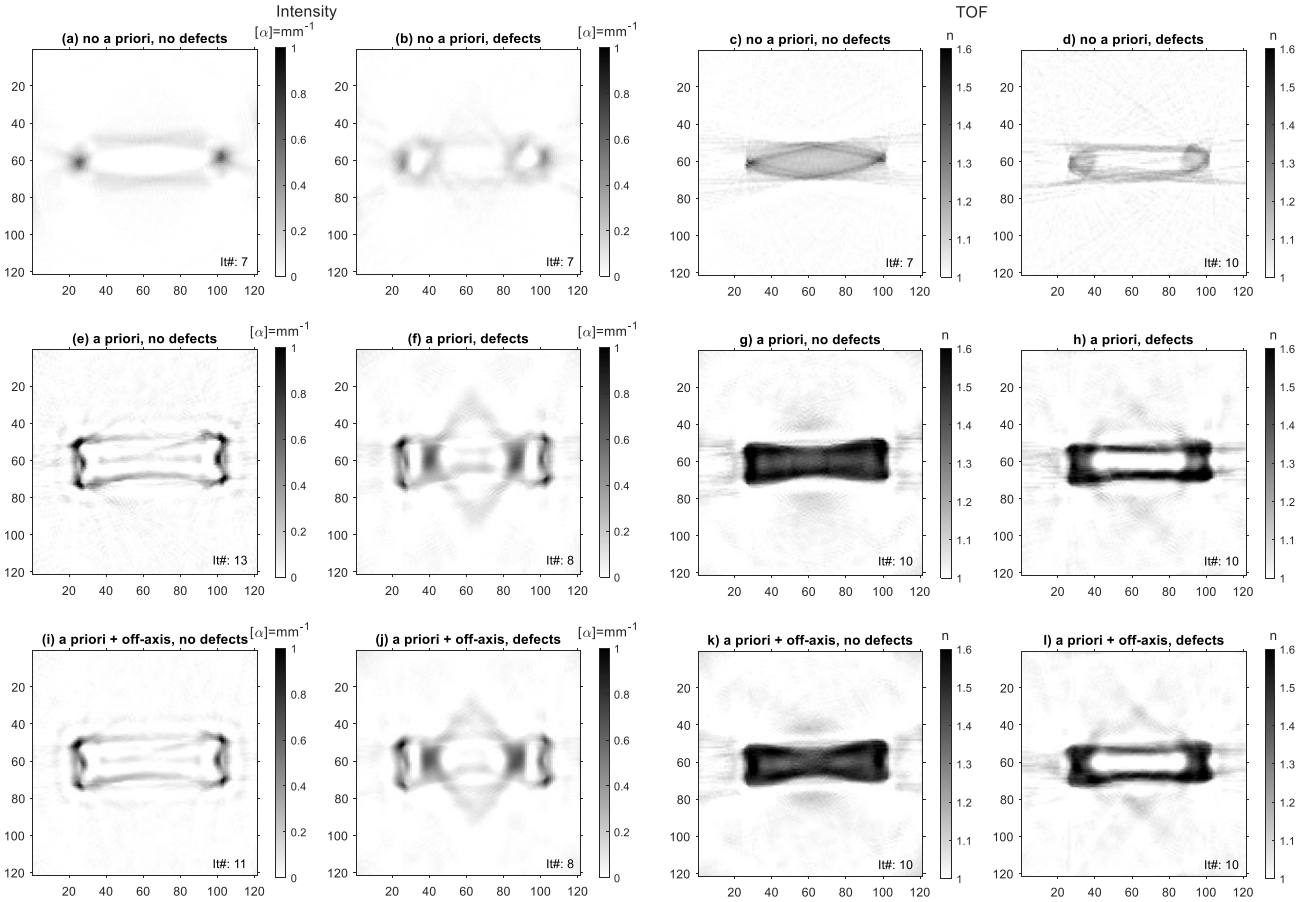

FIGURE 12. Reconstructions of the absorption coefficient α (a,b,e,f,I,j) and the real refractive index n (c,d,g,h,k,l) of Sample 3(a) and 3(b) made out of PE. X- and Y-axis in mm. The reconstructions where performed without a priori information (a)-(d), with method 1 considering beam shape and optical effects (e)-(h), with method 2 additionally including scattered radiation from off-axis measurements (i)-(l). Iteration numbers CGLS reconstruction algorithm are given in the lower right corner.

erroneously interpreted as areas with strong absorption or a high refractive index n, respectively. For the reconstructions from the ToF data, n reaches a value of up to 3 leading to very dark edges (for the expected values refer to Table 1). Additionally, the sharp corners of the samples are not reconstructed, so that the shape of the reconstructed object appears rounded. The defects in Sample 1(b) are visible, but, because their boundaries strongly scatter the radiation, they appear to have a higher absorption value or refractive index than the surrounding material.

We compensate for these effects by applying reconstruction method 1 introducing *a priori* information to the matrix. The visibility of the object's shape in the reconstruction is much better, as depicted in Fig. 9(e)-(h). The corners are distinctively visible in all four reconstructions and the edges of the sample appear less pronounced. In the reconstruction of α from the intensity data of Sample 1(b) (Fig. 9(f)), the defects are still visible as strong absorbers. This is due to the fact, that the outlines of the defects or even their existence were not part of the *a priori* information, so they were not considered in the matrix. This is advantageous for NDT applications because ultimately the goal of NDT is to find defects, whose existence is unknown *a priori*.

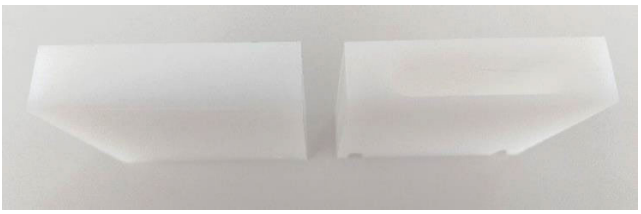

FIGURE 13. Photography of Sample 3 (a) and 3(b) made from Polyethylen (PE): 20 mm × 75 mm × 75 mm (b) drilled-out "defect" ∼ 50 mm × 10 mm.

For the n reconstruction from the TOF of Sample 1(b) (Fig. 9(h)), however, the three defects are perfectly visible as holes in an otherwise uniform block. Although it would be difficult to define the exact outlines of the defects from the reconstruction and thus compare them to their real size, it is obvious that the defects' dimensions appear exaggerated. A possible reason for this could be the fact that the rays that interfere with the defects are the ones that are refracted when traveling through the sample. Therefore, in many cases, they do not reach the detector aperture and their information is not included in the reconstruction. Consequently, it is necessary to consider the deflected radiation as well. We do

this by applying reconstruction method 2 (Fig. 9(i)-(l)). For the sample without defects (Fig. 9(i) and (k)), the uniformity of the reconstruction is improved in comparison to method 1, since the deflected radiation traveling diagonally through the samples is considered in the reconstruction. For Sample 1(b), carrying defects, the reconstruction improves as well. The defects become sharper and more pronounced than before, allowing a clear distinction between a sample with and a sample without defects, especially when one looks at the reconstruction of the refractive index n.

2) SAMPLE 2

The reconstructed images of Samples 2(a) and (b) are displayed in Fig. 10. For the classic reconstruction process without *a priori* information, the deflection of the rays resulting from the optical effects at the sample surface boundaries leads to even worse reconstructions than for Sample 1. The outer surface boundaries are much too pronounced and the corners disappear so that the blocks seem to be round. Again, scattering effects make the defects appear as dark areas in the image, however, for the reconstruction from the ToF data, the low reconstruction quality does not allow distinguishing the holes.

Using *a priori* information improves the reconstruction significantly, similar to Sample 1. Especially in the reconstructions of Sample 2(a) (Fig. 10(e) and 10(g)) the values of α and n are varying less throughout the uniform parts of the object. Two of the three defects of Sample 2(b) are visible in Fig. 10(f) as dark areas. Scattering is likely to be the reason for the cross-shaped artifacts around the defects. In the reconstruction of n (Fig. 10(h)), the defects are visible but very blurry. Their geometric dimensions are too large and their boundaries are not clearly distinguishable. This improves when the scattered radiation is considered. In Fig. 10(l) the defects appear smaller and sharper even though their outlines are still diffuse. In Fig. 10(j), the reconstruction of α, the cross-shaped artifacts are reduced, so that the reconstruction is closer to being uniform in the parts of the sample without defects. The same holds true for Fig. 10(i) and Fig. 10(k), the reconstructions of Sample 2(a) considering *a priori* information and the off-axis measured data. Overall, by combining the results of intensity and ToF reconstructions, the unknown defects can be detected and a better sample representation in the reconstructed image can be achieved. However, the defect size and arrangement bring the measurement setup to its resolution limit, so that one of the defects is only barely visible regardless of the reconstruction method.

3) SAMPLE 3

Regarding its very low absorption coefficient α_{mat} Sample 3 differs drastically from the other two samples. As a result, the intensity decrease of the radiation when traversing the sample is much lower. The Fresnel losses occurring at the sample surface boundary therefore dominate the intensity measurement, which leads to the low reconstruction quality visible in Fig. 12. Neither the consideration of *a priori* information nor the utilization of off-axis data could cope with this effect, completely covering up the relevant information about the sample interior. Solely the outer shape of the sample is visible in Fig. 12(e) and (i). The TOF measurement data on the other hand, since it is not sensitive to Fresnel losses, leads to very good reconstruction results.

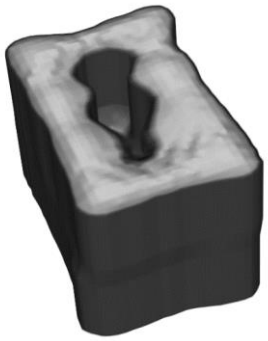

FIGURE 14. 3D reconstruction of Sample 1(b).

The reconstructions from the plain CGLS algorithm show the same problems as before, namely round corners and overly pronounced edges. The "defect" in Fig. 12(d) is visible, but its shape is distorted, as it seems to be a rectangle rather than a pill with round corners. This changes for the reconstructions with method 1 (Fig. 12(g) and (h)). The outer corners of the objects are much sharper and the correct value of $n \approx n_{\text{mat}} = 1.52$ is determined. In addition, the shape of the defect is imaged correctly. On either side of the defect, there are areas erroneously reconstructed with a lower absorption coefficient. These are artifacts, which can be suppressed by considering the off-axis data in the reconstruction. Applying method 2 (Fig. 12(k) and (l)), the solid parts of the samples are reconstructed more precisely and appear more uniform, because radiation traveling diagonally in the sample is considered. The defect is reconstructed by this method with its correct shape, too.

As already stated in [18], when inspecting PE with terahertz tomography one should mainly rely on the ToF data analysis for sample quality evaluation, rather than on the intensity data. The reconstructions of n are more reliable in the case of Sample 3. The good results were improved further by applying methods 1 and 2 displaying the defect within the sample very accurately.

VI. CONCLUSION AND OUTLOOK

We have shown that *a priori* information can have a strong positive impact on the reconstruction quality of terahertz tomography. By including information about the beam shape and optical effects occurring at the sample boundaries, we were able to get largely accurate reconstructions of the samples. We have shown that defects down to a size of 2 mm can be resolved. Even defects whose existence was *not included* in the set of *a priori* information were imaged

more accurately and reliably than it is possible without the application of this new technique. We are able to improve the good results even further by including the analysis of off-axis measurements in the reconstruction. This way deflected radiation is utilized for the reconstruction process, thus sharpening the images of samples and defects. This is also illustrated in Fig. 14, which shows a 3D reconstruction of Sample 1(b) created by combining multiple B-scans (slice images) at different heights of the sample. Since the shapes of the samples under investigation are similar, the differences between the images resulting from the respective reconstruction schemes of samples 1 to 3 mainly result from the different optical properties. This is most evident in the reconstructions from the intensity data, since the samples' absorption coefficents differ substantially. On the other hand, the reconstructions of the real refractive index n (all in the range between 1.5 and 1.7) show similar performance for all three samples.

One drawback of terahertz tomography with off-axis measurements is the long acquisition time. Applying this method the transmitter and the receiver are moving independently from each other along their full range of motion. The acquisition time of one of the cross-section reconstructions seen above is around six hours. This time could be decreased significantly since only a small subset of the acquired data is actually used for the reconstruction, even when applying method 2. Building the sinograms $\vec{b}$ and $\vec{b}_{\mathrm{ASM}}$ in (13) requires only the data acquired by the receiver at the opposite side of the transmitter position and on the position $y_{\max}$, i.e. the receiver position at which the ray tracing simulation predicts the most radiation to be received. Since $y_{\max}$ is determined *a priori*, only the data from these two positions has to be acquired by the receiver.

Acquiring the full range of receiver data, however, gives rise to the opportunity of utilizing even more off-axis data from different positions and thus potentially improving the reconstruction quality further. For future work, we will speed up the acquisition without reducing the field of view. We intend to apply detector arrays [37] covering the full range of the receiver movement simultaneously.

An additional limitation of our current setup that can potentially be tackled with the application of detector arrays, is the limitation of the incident angle. For strongly diverted beams, the receiver lenses fail to guide the radiation to the detector antenna and therefore, method 2 does improve the image quality significantly. Applying detector arrays with a very high acceptance angle per pixel can solve this problem.

Before an image can be reconstructed from the measurement data, the ray-tracing procedure has to be performed. This takes about 2 hours for 180 angles and 100 sampling points on the projection axis to simulate the beam paths. One additional hour has to be invested to build the matrices $\bar{A}$ and $\bar{A}_{\mathrm{ASM}}$. These rough numbers were found on a standard 4-core processor, and could be reduced further by using general-purpose graphics processing units (GPGPU) to perform the highly parallelizable calculations. These procedures have to be performed *only once* for every sample structure or outline and do not have to be repeated for every measurement e.g. in an industrial scenario. They can be stored and utilized for the reconstruction of every sample with the respective outline and material. The calculation of the final reconstruction by CGLS takes about 1s for method 1 and 1.5s for method 2, depending on the number of iterations. The stated values hold for around 10 iterations. In comparison with the measurement time, the evaluation time is therefore negligible.

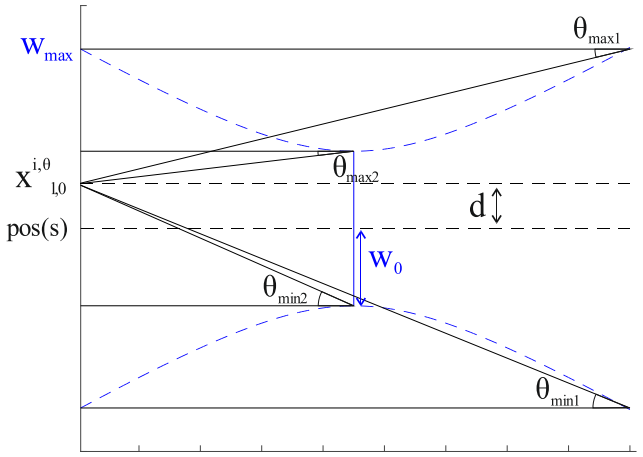

FIGURE 15. Definition of the angles to parametrize the Gaussian beam from several elementary beams.

APPENDIX

In IV-A we introduce the concept of simulating a wide Gaussian beam as a combination of multiple infinitesimal thin elementary beams. We do so by defining a maximum width at the start position $w_{\max} = w(-x_{\mathrm{bound}})$, which can be calculated following (11), where $2{\cdot}x_{\mathrm{bound}}$ is the width of the imaging scene. Elementary rays $\vec{x}^{i,\theta}$ are considered for the reconstruction, if the distance $d = \left|\vec{x}^{i,\theta}_{0,0} - \mathrm{y}_0(s)\right| \leq w_{\max}$. $y_0(s)$ represents the sth sender (and receiver) center position on the y-axis (see Fig. 15). Another condition for an elementary ray to lie within the Gaussian beam is that its starting angle θ fulfills

$$\max(\theta_{\min 1}, \theta_{\min 2}) \leq \theta \leq min(\theta_{\max 1}, \theta_{\max 2}) \tag{14}$$

where:

$$\begin{aligned}
\theta_{\min 1} &= \tan^{-1}\left(-\frac{w_{\max}+d}{2x_{\mathrm{bound}}}\right)\\
\theta_{\min 2} &= \tan^{-1}\left(-\frac{w_0+d}{x_{\mathrm{bound}}}\right)\\
\theta_{\max 1} &= \tan^{-1}\left(\frac{w_{\max}-d}{2x_{\mathrm{bound}}}\right)\\
\theta_{\max 2} &= \tan^{-1}\left(\frac{w_0-d}{x_{\mathrm{bound}}}\right)
\end{aligned} \tag{15}$$

The definitions of the angles are depicted in Fig. 15. The combination of multiple elementary beams to form a Gaussian beam supports our mathematical model of the interaction of the radiation and the sample under test. The good agreement between simulation and measurement, shown in Section V-B. lets us conclude that it approximates the experiment well enough.

REFERENCES

[1] E. Cristofani, F. Friederich, S. Wohnsiedler, C. Matheis, J. Jonuscheit, M. Vandewal, and R. Beigang, "Nondestructive testing potential evaluation of a terahertz frequency-modulated continuous-wave imager for composite materials inspection," *Opt. Eng.*, vol. 53, no. 3, Mar. 2014, Art. no. 031211, doi: 10.1117/1.OE.53.3.031211.

[2] I. Amenabar, F. Lopez, and A. Mendikute, "In introductory review to THz non-destructive testing of composite mater," *J. Infr., Millim., Terahertz Waves*, vol. 34, no. 2, pp. 152–169, Feb. 2013, doi: 10.1007/s10762-012-9949-z.

[3] A. D'Arco, M. D. Di Fabrizio, V. Dolci, M. Petrarca, and S. Lupi, "THz pulsed imaging in biomedical applications," *Condens. Matter*, vol. 5, no. 2, p. 25, Apr. 2020, doi: 10.3390/condmat5020025.

[4] Y. Peng, C. Shi, X. Wu, Y. Zhu, and S. Zhuang, "Terahertz imaging and spectroscopy in cancer diagnostics: A technical review," *BME Frontiers*, vol. 2020, pp. 1–11, Jan. 2020, doi: 10.34133/2020/2547609.

[5] H. Hintzsche, C. Jastrow, T. Kleine-Ostmann, U. Kärst, T. Schrader, and H. Stopper, "Terahertz electromagnetic fields (0.106 THz) do not induce manifest genomic damage in vitro," *PLoS ONE*, vol. 7, no. 9, Sep. 2012, Art. no. e46397, doi: 10.1371/journal.pone.0046397.

[6] M. Naftaly, N. Vieweg, and A. Deninger, "Industrial applications of terahertz sensing: State of play," *Sensors*, vol. 19, no. 19, p. 4203, Sep. 2019, doi: 10.3390/s19194203.

[7] M. Bauer, R. Hussung, C. Matheis, H. Reichert, P. Weichenberger, J. Beck, U. Matuschczyk, J. Jonuscheit, and F. Friederich, "Fast FMCW terahertz imaging for in-process defect detection in press sleeves for the paper industry and image evaluation with a machine learning approach," *Sensors*, vol. 21, no. 19, p. 6569, Sep. 2021, doi: 10.3390/s21196569.

[8] F. Friederich, K. May, B. Baccouche, C. Matheis, M. Bauer, J. Jonuscheit, M. Moor, D. Denman, J. Bramble, and N. Savage, "Terahertz radome inspection," *Photonics*, vol. 5, no. 1, p. 1, Jan. 2018, doi: 10.3390/photonics5010001.

[9] F. Ellrich, M. Bauer, N. Schreiner, A. Keil, T. Pfeiffer, J. Klier, S. Weber, J. Jonuscheit, F. Friederich, and D. Molter, "Terahertz quality inspection for automotive and aviation industries," *J. Infr., Millim., Terahertz Waves*, vol. 41, no. 4, pp. 470–489, Apr. 2020, doi: 10.1007/s10762-019-00639-4.

[10] S. Mohammadzadeh, A. Keil, S. Leuchs, C. Krebs, D. NuBler, J. Seewig, and F. Friederich, "Hand-guided mobile terahertz 3D imaging platform with aspherical telecentric f-θ optics," in *Proc. 18th Eur. Radar Conf. (EuRAD)*, Apr. 2022, pp. 377–380, doi: 10.23919/EuRAD50154.2022.9784526.

[11] T. Wang, K. Wang, K. Zou, S. Shen, Y. Yang, M. Zhang, Z. Yang, and J. Liu, "Virtual unrolling technology based on terahertz computed tomography," *Opt. Lasers Eng.*, vol. 151, Apr. 2022, Art. no. 106924, doi: 10.1016/j.optlaseng.2021.106924.

[12] K. Krugener, E.-M. Stubling, R. Jachim, B. Kietz, M. Koch, and W. Viöl, "THz tomography for detecting damages on wood caused by insects," *Appl. Opt.*, vol. 58, no. 22, p. 6063, Aug. 2019, doi: 10.1364/AO.58.006063.

[13] J. B. Perraud, A. F. Obaton, J. Bou-Sleiman, B. Recur, H. Balacey, F. Darracq, J. P. Guillet, and P. Mounaix, "Terahertz imaging and tomography as efficient instruments for testing polymer additive manufacturing objects," *Appl. Opt.*, vol. 55, no. 13, p. 3462, May 2016, doi: 10.1364/AO.55.003462.

[14] P. Fosodeder, S. Hubmer, A. Ploier, R. Ramlau, S. van Frank, and C. Rankl, "Terahertz computer tomography for plastics extrusion (TACTICS)," presented at the ATTRACT Final Conf., 2020.

[15] S. Wang and X.-C. Zhang, "Pulsed terahertz tomography," *J. Phys. D, Appl. Phys.*, vol. 37, no. 4, pp. 1–36, Feb. 2004, doi: 10.1088/0022-3727/37/4/R01.

[16] J. P. Guillet, "Review of terahertz tomography techniques," *J. Infr., Millim., Terahertz Waves*, vol. 35, no. 4, pp. 382–411, 2014, doi: 10.1007/s10762-014-0057-0.

[17] L. A. Shepp and B. F. Logan, "The Fourier reconstruction of a head section," *IEEE Trans. Nucl. Sci.*, vol. NC-21, no. 3, pp. 21–43, Jun. 1974, doi: 10.1109/TNS.1974.6499235.

[18] K. H. May, A. Keil, G. Von Freymann, and F. Friederich, "The conjugate gradient least square algorithm in terahertz tomography," *IEEE Access*, vol. 9, pp. 142168–142178, 2021, doi: 10.1109/ACCESS.2021.3116801.

[19] L. Ding, K. Xiao, P. Liu, J. Liu, and S. Chai, "Overview and classification of a priori information used in microwave tomography," in *IEEE MTT-S Int. Microw. Symp. Dig.*, Beijing, China, Jul. 2016, pp. 1–2, doi: 10.1109/NEMO.2016.7561616.

[20] K. C. Tam and L. J. Thomas, "Digital tomography incorporating a priori information," in *Review of Progress in Quantitative Nondestructive Evaluation*, D. O. Thompson and D. E. Chimenti, Eds. Boston, MA, USA: Springer, 1990, pp. 407–414, doi: 10.1007/978-1-4684-5772-8_50.

[21] A. Zakaria, A. Baran, and J. LoVetri, "Estimation and use of prior information in FEM-CSI for biomedical microwave tomography," *IEEE Antennas Wireless Propag. Lett.*, vol. 11, pp. 1606–1609, 2012, doi: 10.1109/LAWP.2012.2237537.

[22] A. Fhager and M. Persson, "Using a priori data to improve the reconstruction of small objects in microwave tomography," *IEEE Trans. Microw. Theory Techn.*, vol. 55, no. 11, pp. 2454–2462, Nov. 2007, doi: 10.1109/TMTT.2007.908670.

[23] P. M. V. D. Berg and J. T. Fokkema, "Removal of undesired wavefields related to the casing of a microwave scanner," *IEEE Trans. Microw. Theory Techn.*, vol. 51, no. 1, pp. 187–192, Jan. 2003, doi: 10.1109/TMTT.2002.806900.

[24] G. R. Myers, A. M. Kingston, T. K. Varslot, M. L. Turner, and A. P. Sheppard, "Dynamic tomography with a priori information," *Appl. Opt.*, vol. 50, no. 20, p. 3685, Jul. 2011, doi: 10.1364/AO.50.003685.

[25] B. Recur, J. P. Guillet, I. Manek-Hönninger, J. C. Delagnes, W. Benharbone, P. Desbarats, J. P. Domenger, L. Canioni, and P. Mounaix, "Propagation beam consideration for 3D THz computed tomography," *Opt. Exp.*, vol. 20, no. 6, p. 5817, Mar. 2012, doi: 10.1364/OE.20.005817.

[26] J. Tepe, T. Schuster, and B. Littau, "A modified algebraic reconstruction technique taking refraction into account with an application in terahertz tomography," *Inverse Problems Sci. Eng.*, vol. 25, no. 10, pp. 1448–1473, Oct. 2017, doi: 10.1080/17415977.2016.1267168.

[27] P. Fosodeder, S. Van Frank, and C. Rankl, "Highly accurate THz-CT including refraction effects," *Opt. Exp.*, vol. 30, no. 3, p. 3684, Jan. 2022, doi: 10.1364/OE.444151.

[28] J. Kaipio and E. Somersalo, *Statistical and Computational Inverse Problems*. New York, NY, USA: Springer, 2005.

[29] F. Natterer, *The Mathematics of Computerized Tomography*. Philadelphia, PA, USA: Society for Industrial and Applied Mathematics, 2001. [Online]. Available: https://books.google.de/books?id=gjSO1hLbcD0C

[30] A. C. Kak and M. Slaney, *Principles of Computerized Tomographic Imaging*. Philadelphia, PA, USA: Society for Industrial and Applied Mathematics, 2001, doi: 10.1137/1.9780898719277.

[31] W. Wu, D. Hu, K. An, S. Wang, and F. Luo, "A high-quality photon-counting CT technique based on weight adaptive total-variation and image-spectral tensor factorization for small animals imaging," *IEEE Trans. Instrum. Meas.*, vol. 70, pp. 1–14, 2021, doi: 10.1109/TIM.2020.3026804.

[32] A. Bjorck, *Numerical Methods for Least Squares Problems*. Philadelphia, PA, USA: SIAM Society for Industrial and Applied Mathematics, 1996.

[33] P. C. Hansen, *Rank-Deficient and Discrete Ill-Posed Problems: Numerical Aspects of Linear Inversion*. Philadelphia, PA, USA: SIAM, 1998.

[34] M. R. Hestenes and E. Stiefel, "Methods of conjugate gradients for solving linear systems," *J. Res. Nat. Bureau Standards*, vol. 49, no. 6, p. 409, 1952, doi: 10.6028/jres.049.044.

[35] P. C. Hansen, "The L-curve and its use in the numerical treatment of inverse problems," in *Computational Inverse Problems in Electrocardiology*. Cambridge, MA, USA: MIT Press, 2000.

[36] M. Naftaly, "Terahertz optical materials," in *Proc. Int. Traveling Summer School*, Frankfurt, Germany, 2019, pp. 25–49.

[37] R. Hussung, A. Keil, and F. Friederich, "Handheld millimeter wave imaging system based on a two-dimensional multistatic sparse array," in *Proc. 45th Int. Conf. Infr., Millim., Terahertz Waves (IRMMW-THz)*, Buffalo, NY, USA, Nov. 2020, pp. 1–2, doi: 10.1109/IRMMW-THz46771.2020.9370732.

KARL H. MAY was born in Mannheim, Germany, in 1992. He received the Dipl.-Phys. degree in physics from Technische Universität Kaiserslautern, Kaiserslautern, Germany, in 2017, working on sensor fusion of electronic terahertz FMCW systems, where he is currently pursuing the Ph.D. degree in development of terahertz tomography systems and software.

He joined the Fraunhofer Institute for Industrial Mathematics ITWM, Kaiserslautern, in 2013, as a Research Assistant at the Optimization Department. In 2016, he switched to the Materials Characterization and Testing Department to pursue his Diploma degree. His research interests include (electronic) terahertz transmitters and detectors, broadband antennas, terahertz measurement and applications, data fusion, and tomography reconstruction algorithms.

ANDREAS KEIL (Member, IEEE) was born in Kiel, Germany, in 1975. He received the degree in physics from Christian Albrechts University, Kiel, in 2003, and the Ph.D. degree in quantum information from the National University of Singapore, Singapore, in 2010.

Since 2009, he has been involved in the research and development of terahertz imaging systems; where he is currently with Fraunhofer ITWM. His main research interests include terahertz imaging, image processing algorithms, and high-performance computation on general-purpose graphics processing units.

GEORG VON FREYMANN graduated in physics from Universität Karlsruhe (TH), Karlsruhe, Germany, in 1998. He received the Dr.rer.-nat. degree in physics from TH, in 2001.

In 2002, he was a Postdoctoral Researcher at the Institute of Nanotechnology, Forschungszentrum Karlsruhe, Germany. From 2003 to 2004, he was a Postdoctoral Researcher at the University of Toronto, Canada. From 2005 to 2010, he headed an independent DFG Emmy-Noether Research Group, Institute of Nanotechnology, Karlsruhe Institute of Technology (KIT). Since 2010, he has been a Full Professor of experimental physics with the Technische Universität Kaiserslautern, Germany. Since 2013, he has also been heads the Department of Materials Characterization and Testing, Fraunhofer Institute for Industrial Mathematics ITWM. He is the author of more than 110 articles and more than 15 inventions. He is the co-founder of two companies. His research interests include 3-D laser-lithography, nanophotonics, optical quantum simulators, terahertz technology, and spin-wave optics.

FABIAN FRIEDERICH received the degree in optoelectronics from Aalen University Sciences, Germany, in 2007, and the Ph.D. degree in physics from Goethe University Frankfurt am Main, Germany, for his work in terahertz imaging with the Ultrafast Spectroscopy and Terahertz Physics Group, in 2012.

During his studies, he was also associated with the Centre for Micro-Photonics, Swinburne University of Technology, Melbourne, Australia, and the Laser Zentrum Hannover, Germany. In 2011, he joined the Institute of Technical Physics, German Aerospace Center (DLR), Stuttgart, Germany, to establish laser-based concepts for monitoring space debris. In 2013, he was granted a Fraunhofer Attract Funding to form a new research group in millimeter-wave and terahertz measurement techniques at the Fraunhofer Institute for Physical Measurement Techniques IPM. Since 2017, his group has been with the Fraunhofer Institute for Industrial Mathematics ITWM, Kaiserslautern, pursuing its millimeter-wave and terahertz activities with an even stronger focus on signal and image processing in nondestructive testing. He is an Active Member of the Microwave and Terahertz Methods Technical Committee of the German Society for Non-Destructive Testing (DGZfP) and the VDI/VDE-GMA Technical Committee 8.17 Terahertz Systems of the Association of German Engineers (VDI).